12-28-2021

Solution-processed flexible broadband ZnO photodetector modified by Ag nanoparticles

N. P. Klochko
National Technical University "Kharkiv Polytechnic Institute"

K. S. Klepikova
National Technical University "Kharkiv Polytechnic Institute"

I. V. Khrypunova
National Technical University "Kharkiv Polytechnic Institute"

V. R. Kopach
National Technical University "Kharkiv Polytechnic Institute"

I. I. Tyukhov
San Jose State University, igor.tyukhov@sjsu.edu

See next page for additional authors

Recommended Citation

N. P. Klochko, K. S. Klepikova, I. V. Khrypunova, V. R. Kopach, I. I. Tyukhov, S. I. Petrushenko, S. V. Dukarov, V. M. Sukhov, M. V. Kirichenko, and A. L. Khrypunova. "Solution-processed flexible broadband ZnO photodetector modified by Ag nanoparticles" *Solar Energy* (2021): 1-11. https://doi.org/10.1016/j.solener.2021.12.051

Solar Energy 232 (2022) 1–11

Contents lists available at ScienceDirect

Solar Energy

journal homepage: www.elsevier.com/locate/solener

Solution-processed flexible broadband ZnO photodetector modified by Ag nanoparticles

N.P. Klochko [a], K.S. Klepikova [a], I.V. Khrypunova [a], V.R. Kopach [a], I.I. Tyukhov [b,*], S. I. Petrushenko [c], S.V. Dukarov [c], V.M. Sukhov [c], M.V. Kirichenko [a], A.L. Khrypunova [a]

[a] National Technical University "Kharkiv Polytechnic Institute", 2, Kirpichov st., 61002 Kharkiv, Ukraine
[b] San Jose State University, Department of Mechanical Engineering, One Washington Square, San Jose, CA 95192-0087, USA
[c] V. N. Karazin Kharkiv National Universit, 4, Svobody Square, 61022, Kharkiv, Ukraine

ARTICLE INFO

Keywords:
Zinc oxide nanostructured layer
Flexible broadband photodetector
Silver nanoparticle
External quantum efficiency
Specific detectivity

ABSTRACT

In this work, we present flexible broadband photodetectors (PDs) fabricated by a deposition of nanostructured zinc oxide (ZnO) films on polyimide (PI) substrates by using cheap and scalable aqueous method Successive Ionic Layer Adsorption and Reaction (SILAR). In order to increase the long-wavelength absorption of the nanostructured ZnO layer, we created its intrinsic defects, including oxygen vacancies by post-treatment at 300 °C in vacuum and thus the light-sensitive material ZnO/PI was obtained. Then we applied silver nanoparticles (Ag NPs) from a silver sol onto a nanostructured ZnO film, which were visualized using SEM in the form of spheres up to 100 nm in size that increased the photocurrent and figures of merit of thus obtained light-sensitive material ZnO_Ag/PI due to localized surface plasmon resonance and double Schottky barriers at the Ag-ZnO interface. To fabricate photodetectors based on a photoconductive effect, these ZnO/PI and ZnO_Ag/PI materials were equipped with ohmic aluminum contacts. The spectral responsivity (R_λ up to 275 A/W to UV light) of solution-processed flexible broadband photodetector based on ZnO_Ag/PI material at different wavelengths of light and light power densities is better than R_λ of the ZnO/PI photodetector, and at least an order of magnitude higher than R_λ of photodetectors based on nanostructured zinc oxide described in recent articles. The external quantum efficiency (*EQE*) of both PDs in this study in UV–Vis-NIR spectra is very high in the range from $1{\cdot}10^2$ to $9{\cdot}10^4$ % and is better or of the same order of magnitude as the *EQE* data of modern flexible broadband high-sensitivity PDs based on nanostructured heterostructures containing ZnO. The specific detectivity in UV–Vis-NIR spectra is large for ZnO/PI (from $3.5{\cdot}10^{10}$ to $1{\cdot}10^{12}$ Jones) and especially for ZnO_Ag/PI (from $1.6{\cdot}10^{11}$ to $8.6{\cdot}10^{13}$ Jones), which indicates the ability of the PDs based on light-sensitive materials ZnO/PI and ZnO_Ag/PI to recognize a very weak light signal.

1. Introduction

Currently, light detecting and harvesting are two noteworthy photoelectric-conversion processes for exploiting the arriving solar energy (Luo et al., 2017; Patel et al., 2020; Tang et al., 2020; Zhang al., 2021). Photodetectors (PDs) that capture light signals and convert them into electrical signals are important functional units in various energy systems. Among them, broadband photodetectors that can detect light from ultraviolet (UV) to visible (Vis) and to near-infrared (NIR) range have become a hot topic recently, because they are critical for color imaging, optical communication, environmental monitoring, medical instruments and day/night-time surveillance (Luo et al., 2017; Liu et al., 2018; Peng et al., 2018; Tang et al., 2020; Zhu et al., 2020; Yu et al., 2021). Flexible PDs, which can be folded and wrapped around curved substrates, are of particular interest for wearable and mobile applications. The ability of flexible photodetectors to detect light at an oblique angle is another advantage for optoelectronic applications such as photovoltaic devices, omnidirectional cameras, optical tracking systems, and optical field measurements (Lee et al., 2017; Luo et al., 2017; Lien et al., 2018; Peng et al., 2018; Wang et al., 2020; Zhu et al., 2020; Yu et al., 2021; Zhang al., 2021). As a direct bandgap semiconductor material, zinc oxide (ZnO) has the characteristics of a wide bandgap (~3.37 eV at room temperature), environmental-friendliness, high mechanical robustness and excellent thermal stability. Therefore, ZnO-

* Corresponding author.
E-mail address: ityukhov@yahoo.com (I.I. Tyukhov).

https://doi.org/10.1016/j.solener.2021.12.051
Received 13 October 2021; Received in revised form 19 December 2021; Accepted 21 December 2021
Available online 28 December 2021

based PDs have attracted wide attention and have become one of the research hotspots in the field of wide-gap semiconductor UV photodetectors (Lee et al., 2017; Lien et al., 2018; Xu et al., 2019; Wang et al., 2020). Since commercial photodetectors have some disadvantages in terms of relatively narrow response spectra and high cost due to a complex manufacturing process that severely limits their widespread use, PDs with solution-processed nanostructured zinc oxide layers are of particular interest (Luo et al., 2017; Lee et al., 2017; Xu and Lin, 2020). Lee et al. (2017) demonstrated flexible UV photodetectors based on ZnO nanostructures synthesized by hydrothermal growth on two-dimensional graphene and molybdenum (IV) sulfide (MoS_2) layers. Lien et al. (2018) showed a wrappable UV photodetector (PD) constructed using an interlaced array of ZnO nanowires as the active material and Ag nanowires as electrodes, both embedded in a thermoplastic polyurethane substrate using printing approaches. Wang et al. (2020) successfully fabricated a flexible ZnO UV photodetector by inkjet printing on polyimide (PI) substrates, which was modified with Ag nanoparticles (NPs) to further improve its performance. According to the analysis by Wang et al. (2020), inkjet-printed silver nanoparticles play a role in the passivation of surface defects in ZnO materials, which reduces the dark current and the decay time of the photodetector. On the other hand, Ag NPs can also work as surface plasmons, which increase the photocurrent of the photodetector due to localized surface plasmon resonance (LSPR) (Chen et al., 2015; Wang et al., 2020). To expand the sensitivity range of a photodetector, Peng et al. (2018) developed a heterostructure based on lead (II) sulfide (PbS) quantum dots and ZnO nanoparticles deposited by spin coating on polyethylene terephthalate substrates, and thus obtained high-performance and broadband flexible UV–Vis-NIR photodetector. Liu et al. (2018) fabricated an ultrasensitive ZnO-based photodetector operating in a broadband wavelength range using gold (Au) plasmonic nanostructures. For this, the authors Liu et al. (2018) deposited films of colloidal ZnO quantum dots by centrifugation and created self-assembled island nanostructures of Au as nanoantennas, which significantly improved the photoresponse of a ZnO-based photodetector in the entire broad spectrum between UV and visible regions due to enhanced light absorption caused by LSPR. According to Tang et al. (2020), plasmonic metallic nanostructures such as silver nanoparticles can absorb incident light in an extended spectral range. In plasmonic Ag NPs, the surface plasmon resonance decays and generates hot electrons. To extend the spectral range of photodetection, hot electrons are used to amplify or to generate internal photoemission and transfer absorbed light energy to neighboring semiconductors, functioning as a "plasmon photosensitizer", thereby providing photoconductivity modulation for PD (Tang et al., 2020). In addition, plasmonic hot electrons can participate in the photocurrent to increase the intensity of the photoresponse, which leads to an increase in the sensitivity of photodetectors (Tang et al., 2020).

In this work, to create a flexible broadband photodetector, we used an inexpensive large-scale wet chemical production method Successive Ionic Layer Adsorption and Reaction (SILAR) to deposit nanostructured ZnO films on PI substrates. Then, in order to increase the long-wavelength absorption of the nanostructured ZnO layer, we in accordance with Wang et al. (2018) created its intrinsic defects, including an oxygen vacancy (V_O), and made ZnO with a high V_O content by post-treatment at 300 °C in a vacuum, thus obtaining a light-sensitive ZnO/PI material. Next, we applied Ag NPs from a silver sol to a nanostructured ZnO film, as described by Bonsak et al. (2010); Klochko et al. (2018), and obtained a light-sensitive material ZnO_Ag/PI. According to Klochko et al. (2018), the Ag nanoparticles created in this way on the surface of electrodeposited nanostructured ZnO films had different shapes and an average size of 60 nm. In addition to surface plasmon resonance, they provided double Schottky barriers on Ag-ZnO interface and ZnO grain boundaries, thereby enhancing the separation of photogenerated electron-hole pairs. Since these barriers effectively prevented the recombination of photogenerated electron-hole pairs, they increased the UV photosensitivity of Ag/ZnO nanocomposites compared to the initial ZnO (Klochko et al., 2018). Here we investigated the crystal structure, surface morphology, chemical composition and optical properties of the light-sensitive materials ZnO/PI and ZnO_Ag/PI. Equipping these materials with ohmic Al contacts, we obtained two solution-processed flexible broadband photodetectors based on ZnO films deposited through SILAR on PI substrates with and without Ag NPs, and compared their figures of merit in UV–Vis-NIR spectra, such as the photocurrent to dark current ratio (*PDCR*), spectral responsivity (R_λ), external quantum efficiency (*EQE*) and specific detectivity (D^*).

2. Experimental procedures

Here, for the manufacture of flexible thin-film photodetectors based on nanostructured ZnO layers with and without Ag NPs, we used polyimide (PI, Kapton-HN®) substrates with a thickness of 25 μm and an area of 4 × 2 cm^2. All chemicals supplied by Sigma-Aldrich for our experiments were of analytical grade and used without further purification. Before applying thin ZnO films to both sides of polyimide substrates by the SILAR method, the substrates were first cleaned in a detergent solution and then rinsed under running distilled water. Thereafter, the PI substrates were treated for 10 min in an ultrasonic bath containing distilled water at 20 °C, boiled in distilled water for 15 min, and dried with hot air.

Then, the seed layers were applied to the cleaned PI substrates by dip coating, as shown schematically in Fig. 1 (a). For this, a seed solution containing a zinc complex ($Zn(NH_3)_4^{2+}$) was prepared by dissolving 0.05 M ZnO in a 1 M aqueous solution of NH_4OH. Then, the PI substrate was immersed in the seed solution for 20 s (1), in hot (95 °C) distilled water for 20 s (2), in cold (20 °C) distilled water for 5 s (3) and dried in a stream of hot air (4). This process was repeated 10 times to obtain ZnO seed layers that evenly covered the PI surface.

Subsequently, thin ZnO films were grown on seeded substrates using the SILAR method, as shown schematically in Fig. 1 (b). For better clarity, the colors of the samples in Fig. 1 are bright, they do not correspond to the real ones. An aqueous solution of a cationic precursor for SILAR deposition of ZnO films contained 0.8 M NH_4OH and 1 M $ZnSO_4$. One growth cycle consisted of the following three steps: (1) immersion of the PI substrate in the cationic precursor for 10 s; (2) its immediate immersion in the anionic precursor, namely in hot (90 °C) distilled water for 10 s; (3) rinsing the substrate in a separate beaker for H_2O at room temperature for 5 s to remove loosely bound particles. Over 200 SILAR growth cycles, ZnO films were obtained on PI substrates with an average thickness *t* of 1.4 μm, which was determined gravimetrically, taking for the calculation the bulk density of ZnO 5.61 g/cm^3. We used the similar SILAR mode in (Klochko et al., 2019; Klochko et al., 2021) for the deposition of thin ZnO films on PI substrates.

In order to increase the long-wavelength absorption of the thus obtained ZnO/PI light-sensitive material, in accordance with Wang et al. (2018) we created nanostructured zinc oxide films with a high V_O content by post-growth vacuum annealing of ZnO/PI at 300 °C and a residual gas pressure of 10^{-4} Pa for 2 h.

To obtain the light-sensitive material ZnO_Ag/PI, a silver sol was used, the composition and photograph of which in the beaker are shown in Fig. 1 (c). The silver sol was prepared as described by Bonsak et al. (2010) through adding dropwise an aqueous reducing solution of trisodium citrate ($Na_3C_6H_5O_7{\cdot}5.5\ H_2O$) to an aqueous solution of silver nitrate ($AgNO_3$). In a typical experiment, a 0.08 mM silver nitrate aqueous solution was heated to boiling, and then a 38 mM trisodium citrate solution was added dropwise to the boiling solution using a burette. The resulting silver sol contained 0.07 mM $AgNO_3$ and 0.14 mM $Na_3C_6H_5O_7$ and was kept boiling and with vigorous stirring throughout the addition, which lasted 3 min and another 7 min after the addition was complete. Thereafter, the silver sol was cooled to room temperature. The experiments were carried out on the deposition of AgNPs on the ZnO/PI surface (Fig. 1 (c)) by immersing the ZnO/PI material in a silver sol for 30 s at 75 °C (1), followed by drying in air for 30 s (2). This

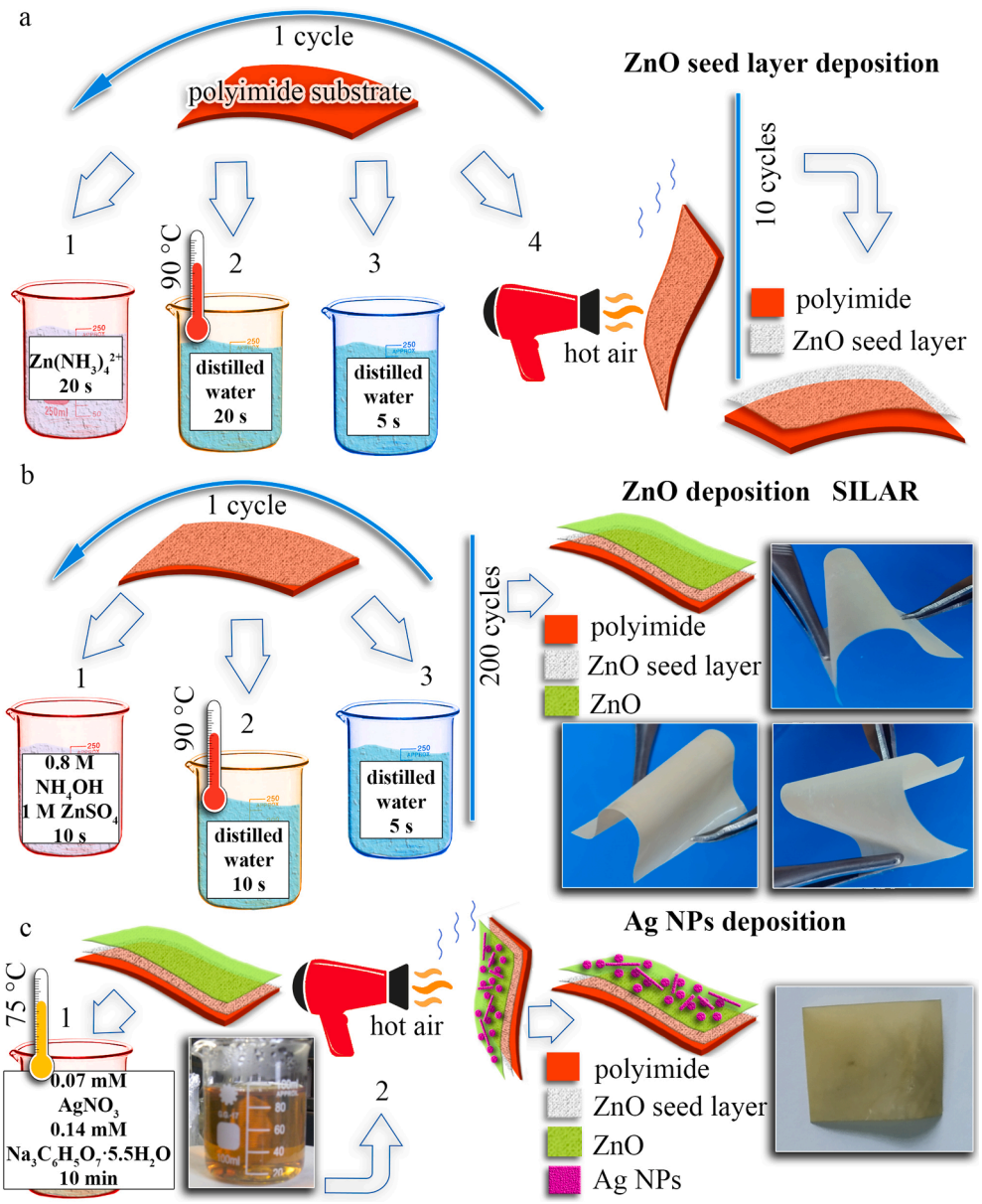

Fig. 1. Schematic representation of the manufacturing process of light-sensitive materials ZnO/PI and ZnO_Ag/PI: (a) deposition of a ZnO seed layer on a PI substrate; (b) - deposition of a nanostructured ZnO layer on the PI substrate coated with seed ZnO layer to obtain a ZnO/PI photosensitive material, and the ZnO/PI photographs; (c) - deposition of silver nanoparticles on the ZnO/PI surface to obtain a photosensitive material ZnO_Ag/PI, and its photograph.

process of deposition of silver nanoparticles was repeated 10 times. Thus, a light-sensitive material ZnO_Ag/PI was obtained, a photograph of which is shown in Fig. 1 (c).

The surface morphology of the light-sensitive materials ZnO/PI and ZnO_Ag/PI was observed using scanning electron microscopy (SEM) in a mode of backscattered electrons (BSE). The SEM instrument "Tescan Vega 3 LMH" operated at an accelerating voltage of 10 kV. Chemical analysis was performed by X-ray fluorescence spectroscopy (XRF) using a "Bruker XFlash 5010" energy dispersive X-ray spectrometer (EDS). Energy dispersion spectra were recorded from areas of 50 × 50 μm. The quantitative assessment of the spectrum was carried out in the self-calibrating mode of the detector.

To analyze the crystal structure of the nanostructured zinc oxide films deposited through SILAR and annealed in vacuum at 300 °C for 2 h in the ZnO/PI and ZnO_Ag/PI samples, X-ray diffraction patterns were recorded on a Shimadzu XRD-6100 X-ray diffractometer with Bragg - Brentano focusing (θ – 2θ). The experimental interplanar spacing d was calculated in accordance with Bragg's law, which describes the condition on θ for the constructive interference to be maximum (Palatnik,1983; Tsybulya and Cherepanova, 2008):

$$n_x\lambda_x = 2d\sin\theta, \quad (1)$$

where n_x is a positive integer and λ_x is the wavelength of the incident X-ray radiation (Cu K_α radiation, $\lambda_x = 0.154060$ nm).

The average crystallite size D or, more precisely, the size of the coherent scattering regions in the direction normal to the reflecting planes of the ZnO film in the ZnO/PI and ZnO_Ag/PI samples was determined by the method of broadening X-ray lines using the Scherer formula:

$$D = (k\cdot\lambda_x)/(\beta\cdot\cos\theta), \quad (2)$$

where k is the Scherer constant ($k = 0.9$); β = (B - b) when B is the observed full width at half maximum (FWHM) and b is the peak broadening due to the instrument in radians ($b = 0.002$ rad), θ denotes the Bragg angle of the X-ray diffraction peak (0 0 2). In addition, to determine the crystallite size D, we used the Williamson-Hall analysis

(Palatnik, 1983), which is a simplified integral width method in which the broadening caused by size and deformation is deconvolved by considering the peak width as a function of 2θ. Microstrains ε in ZnO nanocrystals were calculated as $\varepsilon = \Delta d/d$ (where d is the crystal interplanar spacing according to JCPDS, and Δd is the difference between the corresponding experimental and reference interplanar spacing). Exact experimental values of interplanar spacing were obtained using the Williamson-Hall approximation method described by Palatnik (1983). The lattice constants a and c were identified from the positions of the indexed lines (0 0 2) and (0 0 4) in the X-ray diffraction pattern using the Nelson-Reilly graphical extrapolation method (N-R) and refined using the least squares method with UnitCell software (UC) based on all recorded reflections in the in the X-ray diffraction patterns in accordance with Klochko et al. (2021). The texture quality of the ZnO films in the ZnO/PI and ZnO_Ag/PI materials was assessed using the Harris method (Skompska and Zarębska, 2014). The polar density P_i, which determines the axis of the crystal plane oriented perpendicular to the surface, was calculated using the formula (Skompska and Zarębska, 2014):

$$P_i = (I_i/I_{0i})/[1/\mathrm{N}\sum_{i=1}^{N}(I_i/I_{0i})], \quad (3)$$

where I_i, I_{0i} are the integrated intensity of the i-th diffraction peak of the film and the reference, respectively; N is the number of lines shown in the diffraction. The texture axis has an index that corresponds to the highest P_i value. The orientation factor f for the corresponding direction was calculated using the formula (Klochko et al., 2021):

$$f = \sqrt{1/N\sum_{i=1}^{N}(P_i - 1)^2}. \quad (4)$$

The optical properties of ZnO/PI and ZnO_Ag/PI were studied in the wavelength (λ) range of 400–800 nm using an "SF-2000" spectrophotometer with an "SFO-2000" reflection attachment. Optical reflection measurements were carried out at an angle of incidence of light of 8° relative to the normal to the surface. Light scattering by surfaces was evaluated using the haze factor (H_f), which was calculated as the ratio of the diffuse reflectance R_d to the total reflectance R, where R is the sum of the specular reflectance R_{sp} and R_d. The optical band gap E_g for direct allowed transitions in the ZnO film was determined using the Kubelka-Munk function (Escobedo-Morales et al., 2019):

$$F(R_d) = \frac{(1 - R_d)^2}{2R_d} \quad (5)$$

According to Escobedo-Morales et al.(2019), the plot of $(F(R_d)\cdot h\nu)^2$ vs $h\nu$ gives the value of the direct band gap E_g of ZnO by extrapolating the linear part $(F(R_d)\cdot h\nu)^2$ to $h\nu$.

To fabricate flexible photodetectors based on the photoconductive effect, the light-sensitive materials ZnO/PI and ZnO_Ag/PI were equipped with ohmic aluminum contacts, which were created by vacuum deposition of Al films 300 nm thick at a residual gas pressure 10^{-4} Pa through shadow mask as shown in Fig. 2 (a). To connect the aluminum contacts with the wires of the external circuit, a conductive silver-based glue "Kontaktol" was used. Fig. 2 (a) on the right shows a schematic of a test flexible broadband photodetector of the photoconductor type based on the ZnO_Ag/PI photosensitive material, equipped with a contact chain consisting of seven aluminum strips. The distance between two adjacent aluminum strips l is 2.5 mm, the contact length L is 40 mm. In the experiments, we used both adjacent contacts and any other pair of contacts shown in Fig. 2, taking into account the effective exposure area A between contacts not covered with aluminum. Fig. 2 (b) shows a schematic of a UV–Vis-NIR test setup that contains a set of five Edixeon™ light emitting diodes (LEDs): 365–370 nm LED (UV light); 460–475 nm LED (blue light); 515–535 nm LED (green light); 620–630 nm LED (red light); 930–950 nm LED (near infrared light). The radiation

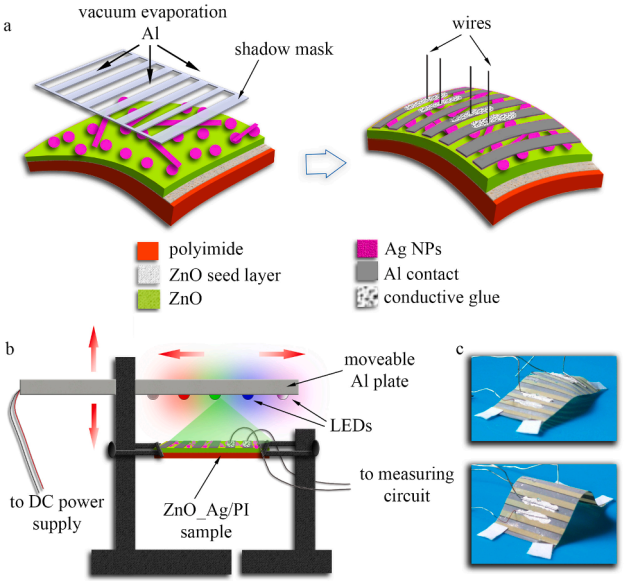

Fig. 2. (a) - Schematic of a test flexible broadband photodetector of the photoconductor type based on the ZnO_Ag/PI photosensitive material, equipped with a contact chain consisting of seven aluminum strips. (b) - Schematic of a UV–Vis-NIR test setup that contains a set of five Edixeon™ light emitting diodes (LEDs): 365–370 nm LED (UV light); 460–475 nm LED (blue light); 515–535 nm LED (green light); 620–630 nm LED (red light); 930–950 nm LED (near infrared light). (c) - Photographs of the fabricated test flexible broadband PD based on ZnO_Ag/PI.

intensity was adjusted in a manner similar to that presented by Zhai et al. (2021) through varying the distance h from LED to tested photodetector, as shown in Fig. 2 (b). In addition, the optical power of the LED was changed by changing its input voltage. The radiation intensity was calculated in accordance with Moreno (2020) using a mathematical model of the illumination diagram at short distances, valid for most LEDs, which simulated the dependence of illumination both on the distance from the LED to the photodetector h, and on the coordinates l and L of the illuminated object. In this study, we used adjustable radiation intensities, or incident illumination power densities (P_λ) from 0.4 to 35.4 mW/cm^2. Fig. 2 (c) shows two photographs of the fabricated test flexible broadband photodetector based on ZnO_Ag/PI.

To characterize and compare the performance of ZnO/PI and ZnO_Ag/PI photodetectors, we studied their time-dependent photoresponse versus illumination wavelength λ, bias voltage U, and radiation power density P_λ, as described by Xu and Lin (2020); Veerla et al. (2017); AlZoubi et al. (2018); Zhou et al. (2019); Patel et al. (2020). The PD sensitivity was calculated according to Veerla et al. (2017); Duan et al. (2019); Zhou et al. (2019) as the ratio of current under illumination to dark current, i.e. photocurrent to dark current ratio:

$$PDCR = (I_{ph}\bullet 100\%)/I_{dark}), \quad (6)$$

where the photocurrent I_{ph} is the difference between the current under illumination I_λ and the current in the dark I_{dark} for given λ, U and P_λ ($I_{ph} = I_\lambda - I_{dark}$).

Then, using the time-dependent photoresponse plots, we calculated the performance metrics of the photodetectors, also called figures of merit. According to Xu and Lin (2020); Veerla et al. (2017); AlZoubi et al. (2018); Zhou et al. (2019); Patel et al. (2020), we obtained the spectral responsivity R_λ as the output current divided by the total light power incident on the photodetector. The spectral responsivity was determined as the ratio of the photocurrent I_{ph} to the product of the radiation intensity P_λ and the effective illumination area (A) of the PD:

$$R_\lambda = I_\lambda/(P_\lambda\cdot A) \quad (7)$$

To validate the performance of the photodetectors developed in this work, we identified two other important parameters for the high

performance photodetectors that were used by Xu and Lin (2020); Zhou et al. (2019); Patel et al. (2020). These are the specific detectivity D^* and external quantum efficiency *EQE*. According to Zhou et al. (2019); Patel et al. (2020), if we assume that I_{dark} is the main contributor to noise, the specific detectivity can quantify the sensitivity of the photodetector and be defined as:

$$D^* = R_\lambda A^{1/2} / (2eI_{dark})^{1/2} \quad (8)$$

where e is the elementary charge.

According to Xu and Lin (2020); Veerla et al. (2017); Zhou et al. (2019); Patel et al. (2020), the external quantum efficiency *EQE*, also called the incident photon-to-current efficiency, determines the number of electrons produced per incident photon. That is, *EQE* is the ratio of photogenerated electrons collected outside the device to the number of incident photons. It was determined by Xu and Lin (2020); Veerla et al. (2017); Zhou et al. (2019); Patel et al. (2020) and is calculated in our study as:

$$EQE = h_p\, c_l\, R_\lambda \cdot 100\% / (\lambda \bullet e), \quad (9)$$

where h_p is Planck's constant and c_l is the speed of light.

3. Results and discussion

Fig. 3 shows the surface morphology of light-sensitive materials ZnO/PI and ZnO_Ag/PI, observed using scanning electron microscopy in the backscattered electron mode. A feature of this shooting mode is the ability to detect atoms with heavier nuclei (zinc of ZnO and silver of AgNPs) against the background of light atoms (carbon of PI). Thus, the "brighter" BSE intensity correlates with the greater average atomic number in the sample (Zn and Ag), while the "dark" areas have lower average atomic number (C, O, etc.). In the SEM images of ZnO shown in Fig. 3, we can see flower-like structures of ZnO with rounded petals, similar to those grown by Garza-Hernández et al. (2017) through the SILAR method, in which cationic solution contained $ZnSO_4$ as a zinc precursor and ammonia as a complexing agent. The authors Garza-Hernández et al. (2017) explained the flower-like shape of ZnO structures by the formation of $Zn(NH_3)^{2+}$ complexes. If a large amount of NH_3 reacts with Zn^{2+} in the positive polar surface, the surface energy of the positive polar planes [0 0 1] decreases, which prevents the growth of ZnO in the (0 0 2) plane. As a result, the ZnO growth process occurs in the middle of the ZnO rod, and the faces of the hexagonal wurtzite crystal form petals (Garza-Hernández et al., 2017).

Comparison of SEM images of ZnO/PI and ZnO_Ag/PI materials shows that during the deposition of silver nanoparticles, a slight etching of nanostructured zinc oxide films is observed due to the acidic environment of the silver sol solution. The appearance of silver nanoparticles in the ZnO_Ag/PI sample in Fig. 3 (b) is visualized as light beads up to 100 nm in size. This is in good agreement with the transmission electron microscopy data, obtained using the SELMI EM 125 TEM instrument in our previous study (Klochko et al., 2018), about the predominantly spherical shape of AgNP with an average size of 60 nm, obtained by the same method from silver sol.

Chemical X-ray fluorescence microanalysis (Fig. 4, Table 1) showed that light-sensitive material ZnO/PI contains Zn and O. The light-sensitive material ZnO_Ag/PI additionally contains < 1 at.% Ag (more precisely 0.02 at.% Ag). In addition to these main elements of the ZnO films and Ag NPs, the XRF spectra contain Al from the vacuum chamber. Carbon and aluminum were excluded from the calculation to obtain the data in Table 1.

The insets in Fig. 4 show the X-ray diffraction patterns of ZnO/PI and ZnO_Ag/PI materials. An analysis of the crystal structure of ZnO films in these light-sensitive materials is presented in Table 1. It is seen in Fig. 4 (insets in (a) and (b)) that ZnO in both samples is single-phase, polycrystalline and has a hexagonal structure of ZnO wurtzite (according to

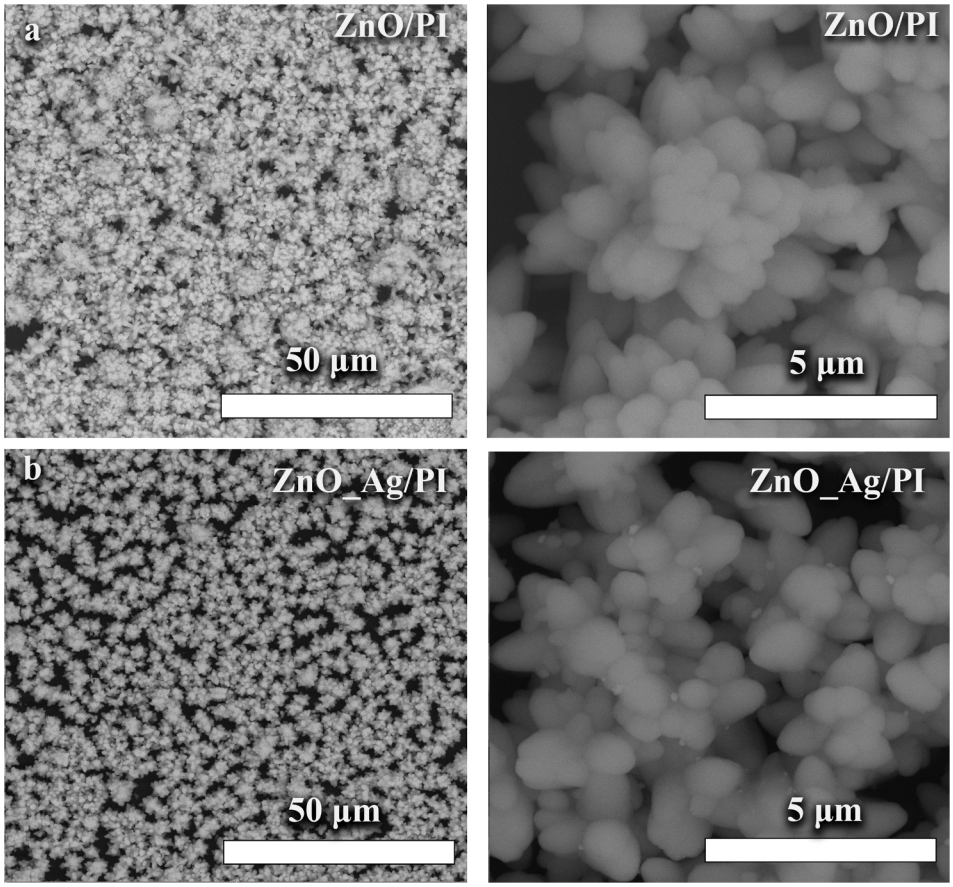

Fig. 3. SEM backscattered-electron imaging of the light-sensitive materials ZnO/PI (a) and ZnO_Ag/PI (b) at various magnifications.

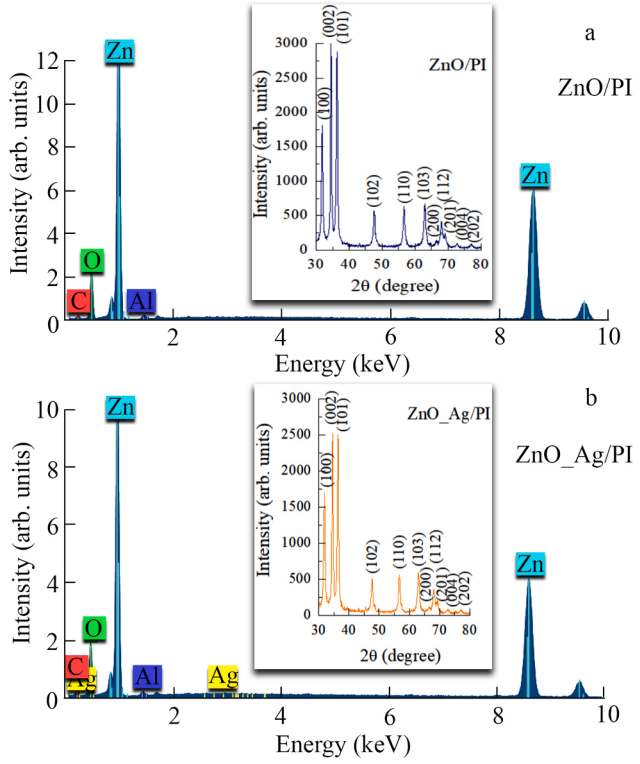

Fig. 4. XRF spectra and XRD patterns (insets) of the light-sensitive materials ZnO/PI (a) and ZnO_Ag/PI (b).

JCPDS #36–1451). Due to the small amount of silver in the ZnO_Ag/PI sample, no extraneous peaks were found in its XRD in Fig. 4 (inset in (b)). Calculations of the grain size of ZnO by the Scherer method and in the Williamson-Hall approximation using broadening of X-ray diffraction peaks gave approximately the same values of D in the range of 24–55 nm (Table 1).

Nanostructured ZnO films in these samples have low microstrains (ε from $1.1{\cdot}10^{-3}$ to $5.3{\cdot}10^{-3}$ arb. units) and a dislocation density $1/D^2$ in the range of $3.3{\cdot}10^{14}$ – $1.7{\cdot}10^{15}$ lines·m^{-2}. The crystal lattice constants a presented in Table 1 are approximately the same as those of the reference ZnO (according to JCPDS #36–1451, $a = 3.246$ Å and $c = 5.206$ Å), as well as according to a comprehensive review of ZnO materials and devices (Özgür et al., 2005). According to Özgür et al. (2005), the lattice constants of ZnO are mainly in the range from 3.2475 to 3.2501 Å for the parameter a and from 5.2042 to 5.2075 Å for the parameter c. However, the c-parameters of the ZnO films in the ZnO/PI and ZnO_Ag/PI samples are lower than the reference parameters given by Özgür et al. (2005). This is one of the reasons for the presence of tensile microstrains and dislocations in zinc oxide films presented in Table 1. As seen in Fig. 4 (insets in (a) and (b)) and in Table 1, ZnO films do not have a pronounced texture in the (0 0 2) plane, the orientation coefficients f are in the range of 0.2–0.3 arb. units.

Fig. 5 (a) shows the optical reflectance spectra of the ZnO/PI and ZnO_Ag/PI samples. These samples are characterized by a high optical diffuse reflectance, which is demonstrated by their haze factors H_f in the range 98–99 % in Fig. 5 (b). As it seen in Fig. 5 (c), the band gap of both ZnO films is about 3.2 eV, which is slightly lower than the characteristic E_g value of zinc oxide 3.37 eV (Jiang et al., 2017; Fortunato et al., 2018). According to Srikant and Clarke (1998), this may be due to the presence of a large number of shallow donor defects such as V_O, and, as a consequence, to the existence of a valence band-donor transition at 3.15 eV.

Fig. 6 shows the time-dependent photoresponses of the ZnO/PI and ZnO_Ag/PI samples depending on the illumination wavelength λ, obtained at a bias voltage $U = 2$ V. Although different radiation intensities P_λ were used, it is clearly visible in Fig. 6 (a), (b) the highest sensitivity of both samples to UV light (λ = 365–370 nm) and blue light (λ = 460–475 nm). The maximum photocurrent I_{ph} of the sample with silver nanoparticles ZnO_Ag/PI is 3 times higher than that of the sample ZnO/PI. According to Liu et al. (2014); Zeng et al. (2016); Klochko et al. (2018); Kwon et al. (2018); Li et al. (2019); Tang et al. (2020), this enhanced photoresponse to UV and blue light can be explained by LSPR in Ag NPs, whose plasmon oscillations lead to stronger scattering and absorption of light in nanostructured semiconducting zinc oxide of the ZnO_Ag/PI material. In addition to LSPR, the Ag NPs create double Schottky barriers on Ag-ZnO interface and at the ZnO grain boundaries, which improve the separation of photogenerated electron-hole pairs and

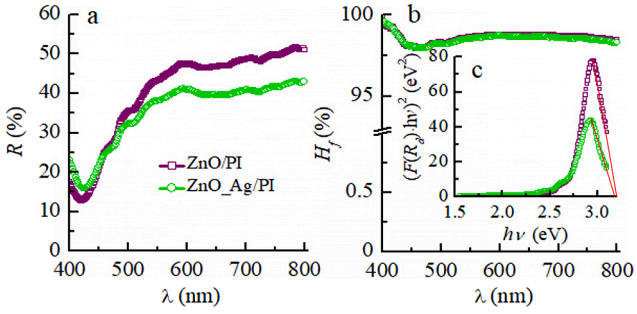

Fig. 5. Optical properties of the ZnO/PI and ZnO_Ag/PI materials: (a) –total reflectance spectra; (b) – Haze factor spectra; (c) – plots for determining the band gap of ZnO using the Kubelka-Munk function.

Table 1
Chemical composition and crystal structure of ZnO films in the light-sensitive materials ZnO/PI and ZnO_Ag/PI.

Sample	Chemical composition according to EDS, at. %			Crystal structure according to XRD									
	Zn	O	Ag	D, nm		$\varepsilon{\cdot}10^3$, arb.units		$1/D^2$, lines·m^{-2}		Texture		Lattice constants, Å*	
				by Scherer	by Williamson-Hall	by Scherer	by Williamson-Hall	by Scherer	by Williamson-Hall	$P_{(hkl)}$ ($h = 0$ $k = 0l = 2$)	f, arb. units	according to N-R	according to UC
												a, Å / c, Å	a, Å / c, Å
ZnO/PI	31	69	–	28	24–37	4.7	1.1–2.5	$7.7{\cdot}10^{14}$	$7.3{\cdot}10^{14}$ – $1.7{\cdot}10^{15}$	1.7	0.3	3.248 / 5.197	3.247 / 5.198
ZnO_Ag/PI	42	58	< 1 (0.02)	24	24–55	5.3	3–4.3	$1.7{\cdot}10^{15}$	$3.3{\cdot}10^{14}$ – $1.7{\cdot}10^{15}$	1.6	0.2	3.251 / 5.177	3.249 / 5.195

* According to JCPDS #36–1451, $a = 3.249$ Å, c = 5.206 Å. The errors of calculation of the lattice constants equal ± 0.005 Å

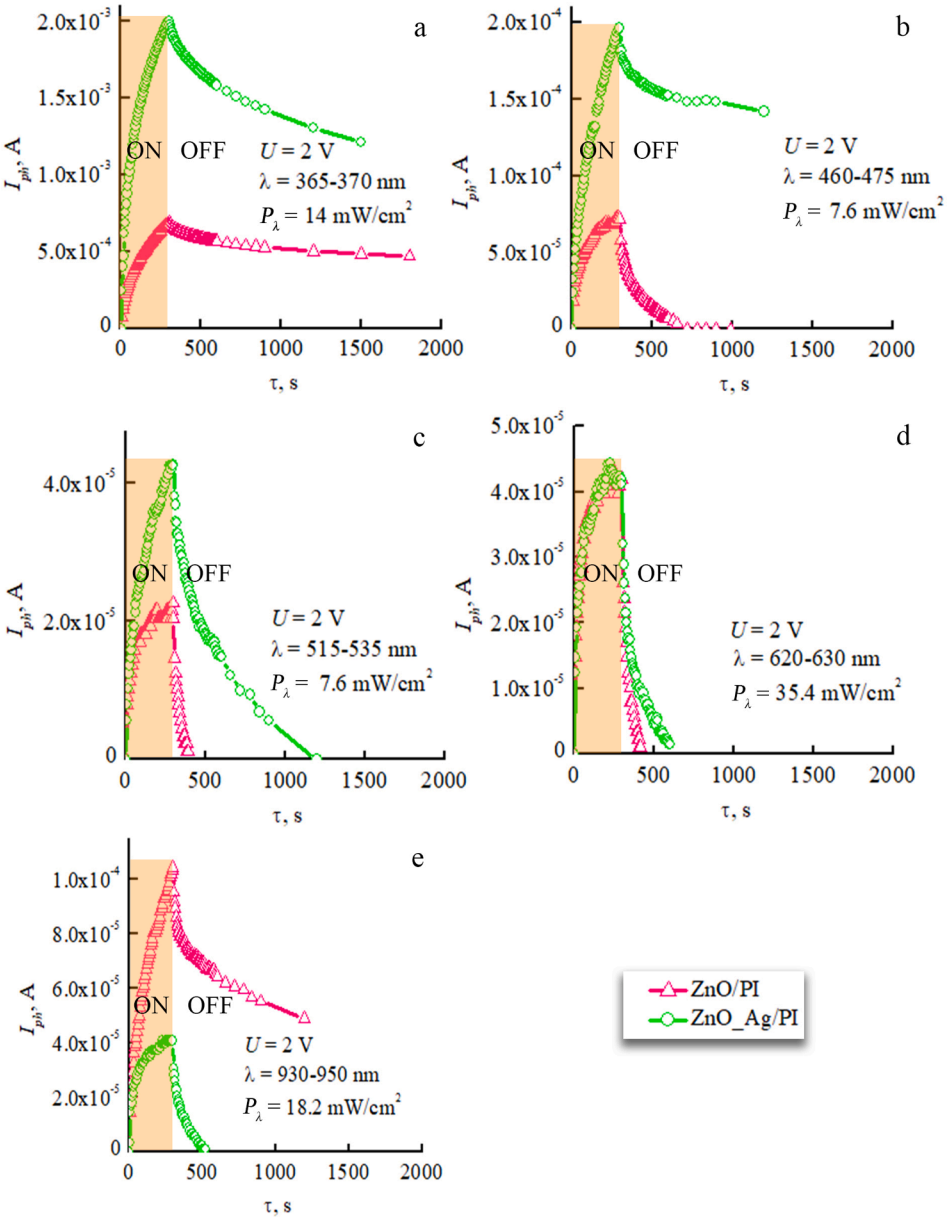

Fig. 6. Light-induced current outputs in real time of solution-processed flexible broadband photodetectors based on ZnO/PI and ZnO_Ag/PI materials at a bias voltage of 2 V and various illumination power densities P_λ and wavelengths λ: (a) - $P_\lambda = 14$ mW/cm^2, λ = 365–370 nm; (b) - $P_\lambda = 7.6$ mW/cm^2, λ = 460–475 nm; (c) - $P_\lambda = 7.6$ mW/cm^2, λ = 515–535 nm; (d) - $P_\lambda = 35.4$ mW/cm^2, λ = 620–630 nm; (e) - $P_\lambda = 18.2$ mW/cm^2, λ = 930–950 nm.

thus effectively prevent their recombination (Klochko et al., 2018).

However, with an increase in the illumination wavelength above 500 nm, the effect of localized surface plasmon resonance due to silver nanoparticles in the ZnO_Ag/PI sample naturally weakens (Zeng et al., 2016; Kwon et al., 2018; Li et al., 2019; Wang et al., 2020). This can be seen in Fig. 6 (c) for green light (λ in the range of 515–535 nm) not only as a decrease in the maximum value of I_{ph}, but also as a reduction in the ratio of maximum photocurrents in the light-sensitive materials based on a nanostructured ZnO layer coated with Ag NPs and bare ZnO, i.e. in ZnO_Ag/PI and ZnO/PI materials, respectively. As it seen in Fig. 6 (d), under red light illumination (λ in the range of 620–630 nm), photoresponses of the ZnO/PI and ZnO_Ag/PI materials are near equal. In the NIR range (λ = 930–950 nm) photoresponses of ZnO/PI is three times more than ZnO_Ag/PI has (Fig. 6 (e)). According to Wang et al. (2020), the better photosensitivity of the ZnO/PI sample compared to ZnO_Ag/PI in Fig. 6 (e) can be explained by the "shading effect" of Ag NPs, which causes a loss of incident light energy.

Moreover, oxygen vacancies that enhance photoresponsive performance of ZnO (Wang et al., 2018; Ling et al., 2019) are partly passivated by Ag NPs (Wang et al., 2020), due to which the photosensitivity of the ZnO_Ag/PI material to near infrared radiation is reduced.

The effect of external voltage on the device performance was investigated at wavelengths of 365–370 nm and at the light power density of 14 mW/cm^2. Fig. 7 shows that at $U = 2$ V the photoresponsive performance of both PDs is optimal. Therefore, the quality parameters of the photodetectors manufactured by us were determined at $U = 2$ V.

As can be seen in Fig. 8 from the plots of the ratio of the current under illumination to the dark current *PDCR* versus λ (a) and *PDCR* versus P_λ (b), the deposition of silver nanoparticles on the surface of nanostructured zinc oxide layer provides an increased photosensitivity of the ZnO_Ag/PI photodetector compared to the ZnO/PI photodetector in the entire investigated UV–Vis-NIR wavelength range, especially at the light power density of more than 7 mW/cm^2. At low P_λ values, the "shading effect" of Ag NPs is manifested. The ratio of the current under

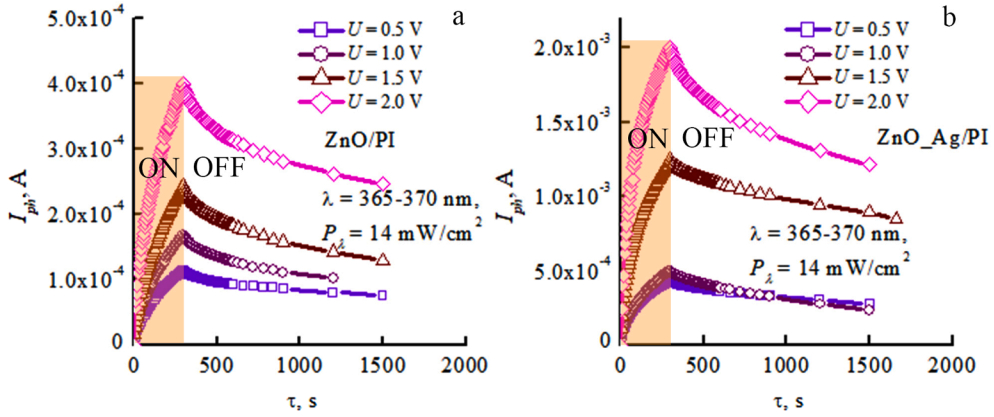

Fig. 7. Light-induced current outputs in real time of solution-processed flexible broadband photodetectors based on ZnO/PI (a) and ZnO_Ag/PI (b) at an illumination power density of 14 mW/cm^2 and wavelengths in the range 365–370 nm and at various bias voltages *U*.

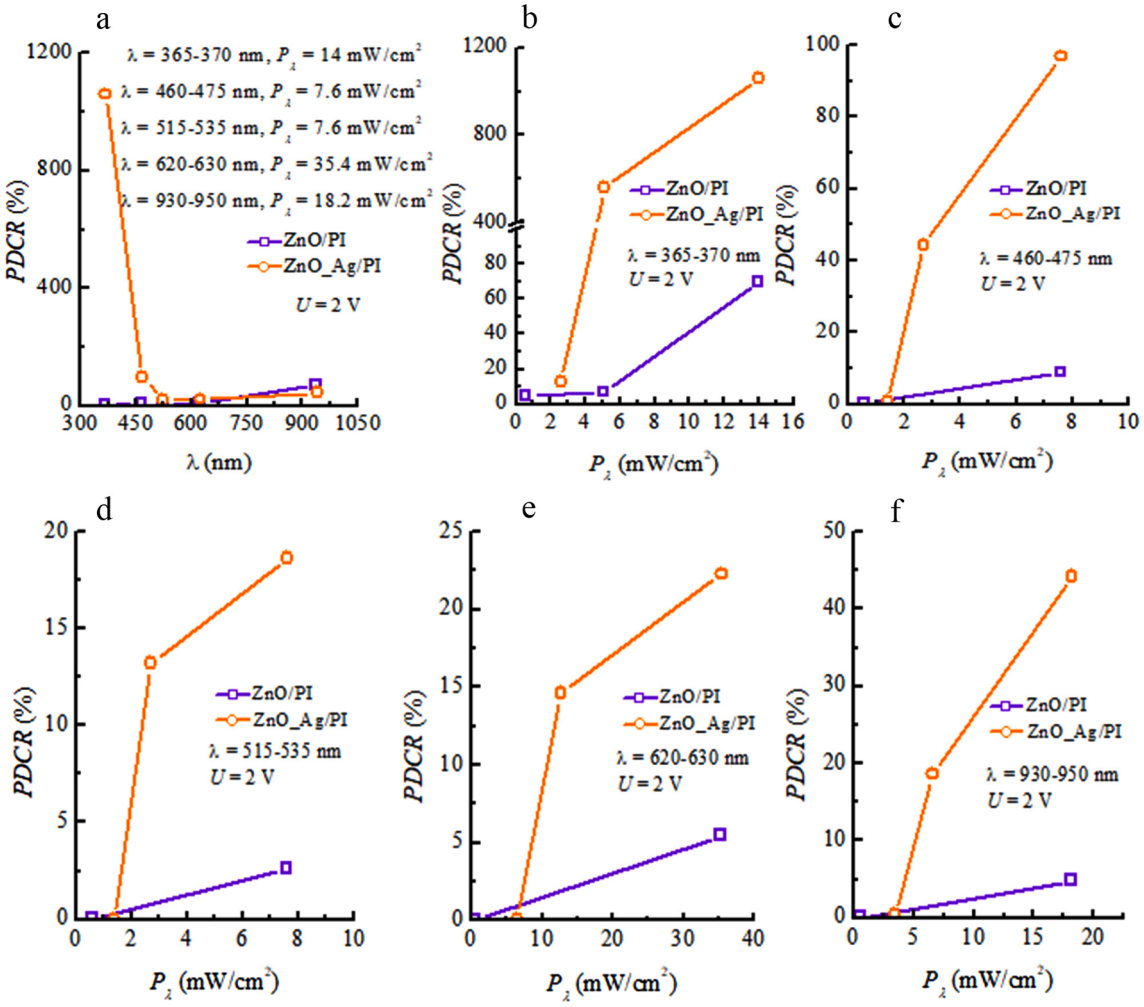

Fig. 8. Photocurrent to dark current ratio (*PDCR*) at a bias voltage 2 V of solution-processed flexible broadband photodetectors based on ZnO/PI and ZnO_Ag/PI materials, depending on the light wavelength (a), the UV light power density (b), the blue light power density (c); the green light power density (d); the red light power density (e); the NIR light power density (f).

illumination to the dark current of both PDs naturally increases with increasing P_λ.

Fig. 9 shows spectral responsivity R_λ of solution-processed flexible broadband photodetector based on ZnO_Ag/PI material at different light wavelength and light power densities, which is better than the R_λ of the ZnO/PI photodetector. As seen in Fig. 9, under ultraviolet light illumination, the R_λ values are especially high: $R_\lambda = 275$ A/W at $P_\lambda = 5.1$ mW/cm^2; $R_\lambda = 205$ A/W at $P_\lambda = 14$ mW/cm^2. These values of R_λ are at least an order of magnitude higher than in recent works of Lien et al. (2018); Xu and Lin (2019); Zhou et al. (2019); Patel et al. (2020); Samanta et al. (2020); Zhang et al. (2021) for ZnO-based UV PDs obtained by different growth and doping methods. Moreover, the R_λ data

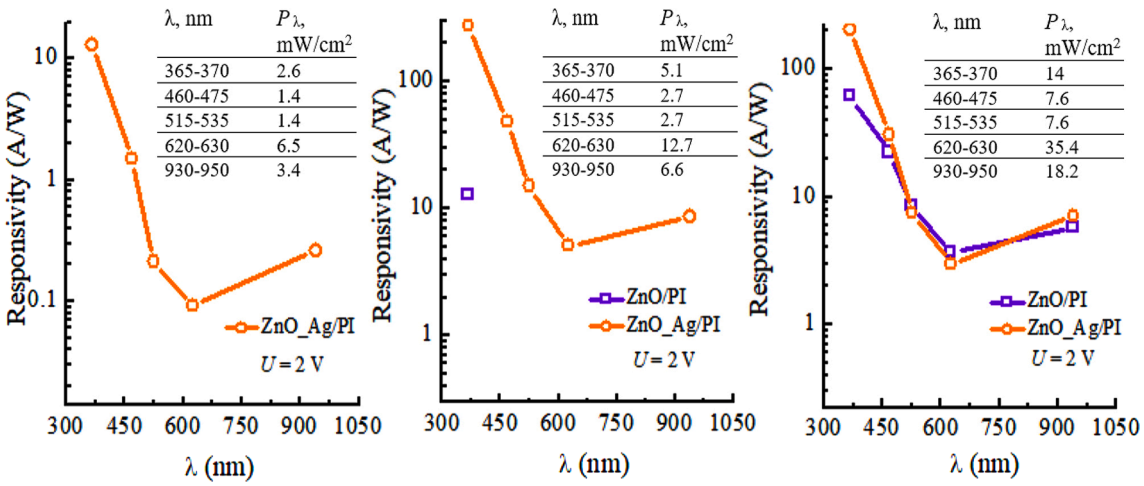

Fig. 9. Spectral responsivity of solution-processed flexible broadband photodetector based on ZnO_Ag/PI material at different light wavelength and light power densities compared to some responsivity data for PD based on ZnO/PI.

for visible and near infrared light presented in this paper for ZnO_Ag/PI PD are also large (Fig. 9) compared to the R_λ of other flexible broadband photodetectors presented by Peng et al. (2018); Zhou et al. (2019) and Samanta et al. (2020). As can be seen in Fig. 9, for blue light $R_\lambda = 48$ A/W at $P_\lambda = 2.7$ mW/cm^2, for green light $R_\lambda = 15$ A/W at $P_\lambda = 2.7$ mW/cm^2, for red light $R_\lambda = 5$ A/W at $P_\lambda = 12.7$ mW/cm^2, and for NIR light $R_\lambda = 9$ A/W at $P_\lambda = 6.6$ mW/cm^2.

Fig. 10 (a) shows the external quantum efficiencies of solution-processed flexible broadband PDs based on ZnO_Ag/PI and ZnO/PI materials at different light wavelengths obtained at a light power density $P_\lambda = 7$ mW/cm^2. In Fig. 10 (a), it can be seen that the maximum *EQE* was obtained for PD based on ZnO_Ag/PI at wavelengths of 365–370 nm. According to calculations using equation (9), all *EQEs* of both PDs in this study in UV–Vis-NIR spectra are very high in the range from $1{\cdot}10^2$ to $9{\cdot}10^4$ %. This is much higher than the *EQE* of broadband high-sensitivity PDs based on heterostructures of colloidal ZnO quantum dots/self-assembled Au nanoantennas (Liu et al., 2018) and *EQE* of UV–visible photodetector based on a I-type heterostructure of ZnO quantum dots/monolayer MoS_2 (Zhou et al., 2019). The *EQE* data of the solution-processed flexible broadband ZnO_Ag/PI photodetector presented in this study is of the same order of magnitude as the *EQE* data reported by Lee et al. (2017) for dimensional-hybrid structures of 2D materials with ZnO nanostructures, as well as Patel et al. (2020) for a PD based on a $ZnOWS_2$/Si heterojunction.

As seen in Fig. 10 (b), the specific detectivity in the UV–Vis-NIR spectra is very high for ZnO/PI (from $3.5{\cdot}10^{10}$ to $1{\cdot}10^{12}$ Jones) and especially for ZnO_Ag/PI (from $1.6{\cdot}10^{11}$ to $8.6{\cdot}10^{13}$ Jones). These values indicate the ability of PDs based on the light-sensitive materials ZnO/PI and ZnO_Ag/PI to recognize a very weak light signal (Wang et al., 2020; Yu et al., 2021). Fig. 10 (b) shows that the maximum D^* value was obtained for PD based on ZnO_Ag/PI at wavelengths 365–370 nm. Nevertheless, all of the D^* data obtained in this study in UV–Vis-NIR spectra have been shown in Fig. 10 (b) are better than those of the photodetectors based on nanostructured zinc oxide described in recent articles by Liu et al. (2018) and Zhou et al. (2019), as well as D^* data for high-performance flexible and broadband photodetectors based on the heterostructure of PbS quantum dots/ZnO nanoparticles (Peng et al., 2018). In addition, the specific detectivity of the ZnO_Ag/PI based PD developed in this work is higher than the D^* shown by Wang et al. (2020) for flexible UV-PD with ZnO modified by Ag nanoparticles, than the D^* presented by Patel et al. (2020) for a broadband and highly sensitive photodetector based on ZnO-WS_2/Si heterojunction, as well as the D^* of the solution-processed flexible $MAPbI_3$ photodetector with ZnO Schottky contact (Yu et al., 2021).

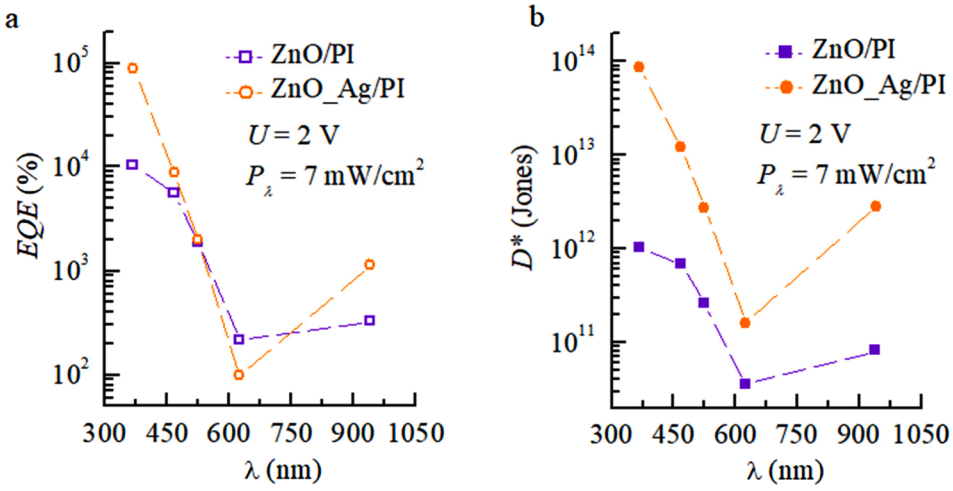

Fig. 10. External quantum efficiency *EQE* (a) and specific detectivity D^* (b) of solution-processed flexible broadband PDs based on ZnO_Ag/PI and ZnO/PI materials obtained at a light power density $P_\lambda = 7$ mW/cm^2 and at different light wavelengths.

4. Conclusions.

In summary, the ZnO/PI light-sensitive material for a flexible broadband photodetector was fabricated using the aqueous SILAR method by deposition the ZnO layer ~ 1.4 μm thick with rounded petal flower nanostructures on the polyimide substrate 25 μm thick, followed by processing at 300 °C in vacuum to enrich ZnO with intrinsic defects such as oxygen vacancies. The average grain size of ZnO is in the range of 24–55 nm, tensile microstrains are from $1.1{\cdot}10^{-3}$ to $5.3{\cdot}10^{-3}$ arb. units, and the dislocation densities are in the range of $3.3{\cdot}10^{14} - 1.7{\cdot}10^{15}$ lines·m^{-2}. The optical band gap of ZnO is about 3.2 eV, which is slightly lower than the characteristic E_g value of zinc oxide 3.37 eV and may be associated with the presence of a large number of shallow donor defects such as V_O, and, as a consequence, with the presence of the valence band-donor transitions at 3.15 eV. To increase the photosensitivity, silver nanoparticles were used, which visualized using SEM in the form of spheres up to 100 nm in size. The Ag NPs were deposited from a silver sol on the ZnO surface, and thus the photosensitive material ZnO_Ag/PI was obtained. For the manufacture of photodetectors based on the effect of photoconductivity, both materials ZnO/PI and ZnO_Ag/PI were equipped with ohmic aluminum contacts by vacuum deposition of Al film strips. The study shows an increased photoresponse of the ZnO_Ag/PI photodetector in comparison with the ZnO/PI photodetector in the wavelength range 365–535 nm due to localized surface plasmon resonance and double Schottky barriers at the Ag-ZnO interface at the ZnO grain boundaries. The better photoresponse of the ZnO/PI sample in comparison with ZnO_Ag/PI to near infrared radiation is explained by the "shading effect" of Ag NPs and the passivation of V_O in ZnO with Ag NPs. The spectral responsivity (R_λ up to 275 A/W at $\lambda = 365–535$ nm) of solution-processed flexible broadband photodetector based on ZnO_Ag/PI material at different wavelengths of light and light power densities is better than R_λ of the ZnO/PI photodetector, and at least an order of magnitude higher than R_λ of photodetectors based on nanostructured zinc oxide described in recent articles. The external quantum efficiency of both PDs in this study in UV–Vis-NIR spectra is very high in the range from $1{\cdot}10^2$ to $9{\cdot}10^4$ % and is better or of the same order of magnitude as the *EQE* data of modern flexible broadband high-sensitivity PDs based on nanostructured heterostructures containing ZnO. The specific detectivity in UV–Vis-NIR spectra is very high for ZnO/PI (from $3.5{\cdot}10^{10}$ to $1{\cdot}10^{12}$ Jones) and especially for ZnO_Ag/PI (from $1.6{\cdot}10^{11}$ to $8.6{\cdot}10^{13}$ Jones), which indicates the ability of the PDs with light-sensitive materials ZnO/PI and ZnO_Ag/PI to recognize a very weak light signal.

Declaration of Competing Interest

The authors declare that they have no known competing financial interests or personal relationships that could have appeared to influence the work reported in this paper.

Acknowledgments

The authors are grateful to the Ministry of Education and Science of Ukraine for financial support of this work. The authors would also like to thank National Research Foundation of Ukraine (NRFU) for financial support of experimental works on manufacturing and research of ZnO films under Grant Number: 128/02.2020.

References

AlZoubi, T., Qutaish, H., Al-Shawwa, E., Hamzawy, S., 2018. Enhanced UV-light detection based on ZnO nanowires/graphene oxide hybrid using cost-effective low temperature hydrothermal process. Optical Materials 77, 226–232. https://doi.org/10.1016/j.optmat.2018.01.045.

Bonsak, J., Mayandi, J., Thøgersen, A., Stensrud Marstein, E., Mahalingam, U., 2010. Chemical synthesis of silver nanoparticles for solar cell applications. Physica Status Solidi (c) 8 (3), 924–927. https://doi.org/10.1002/pssc.201000275.

Chen, H., Liu, K., Hu, L., Al-Ghamdi, A.A., Fang, X., 2015. New concept ultraviolet photodetectors. Materials Today 18 (9), 493–502. https://doi.org/10.1016/j.mattod.2015.06.001.

Duan, Y., Cong, M., Jiang, D., Zhang, W., Yang, X., Shan, C., Zhou, X., Li, M., Li., Q., 2019. ZnO thin film flexible UV photodetectors: regulation on the ZnO/Au interface by piezo-phototronic effect and performance outcomes. Advanced Materials Interfaces, 6(16), 1900470-1-1900470-8. https://doi.org/10.1002/admi.201900470.

Escobedo-Morales, A., Ruiz-López, I.I., Ruiz-Peralta, M.deL., Tepech-Carrillo, L., Sánchez-Cantú, M., Moreno-Orea, J.E., 2019. Automated method for the determination of the band gap energy of pure and mixed powder samples using diffuse reflectance spectroscopy. Heliyon 5 (4), e01505. https://doi.org/10.1016/j.heliyon.2019.e01505.

Fortunato, M., Chandraiahgari, C.R., De Bellis, G., Ballirano, P., Soltani, P., Kaciulis, S., Caneve, L., Sarto, F., Sarto, M.S., 2018. Piezoelectric thin films of ZnO-nanorods/nanowalls grown by chemical bath deposition. IEEE Trans. Nanotechnol. 17 (2), 311–319.

Garza-Hernández, R., Alfaro-Cruz, M.R., Pineda-Aguilar, N., Rivas-Aguilar, M.E., Quevedo López, M., Martínez-Guerra, E., Aguirre-Tostado, F.S., 2017. Growth of lily flower-like ZnO structures by Successive Ionic Layer Adsorption and Reaction method / A. Practical Approaches to Applied Research and Education. Formatex Research Center.

Jiang, Y., Liu, X., Cai, F., Liu, H., 2017. Direct growth of feather-like ZnO structures by a facile solution technique for photo-detecting application, Nanoscale Res Lett., 12 (1), 483-1- 483-6. https://doi.org/10.1186/s11671-017-2252-0.

Klochko, N.P., Klepikova, K.S., Petrushenko, S.I., Kopach, V.R., Khrypunov, G.S., Korsun, V.E., Lyubov, V.M., Kirichenko, M.V., Dukarov, S.V., Khrypunova, A.L., 2018. Nanostructured ZnO arrays fabricated via pulsed electrodeposition and coated with Ag nanoparticles for ultraviolet photosensors. Journal of Nano- and Electronic. Physics 10 (3), 03027-1–03027-8.

Klochko, N.P., Klepikova, K.S., Petrushenko, S.I., Dukarov, S.V., Kopach, V.R., Khrypunova, I.V., Zhadan, D.O., Lyubov, V.M., Khrypunova, A.L., 2019. Effect of high doses of electron beam irradiation on structure and composition of ZnO films prepared by electrochemical and wet chemical depositions on solid and flexible substrates. Radiat. Phys. Chem., 164, 108380-1–108380-10. https://doi.org/10.1016/j.radphyschem.2019.108380.

Klochko, N.P., Klepikova, K.S., Khrypunova, I.V., Zhadan, D.O., Petrushenko, S.I., Kopach, V.R., Dukarov, S.V., Sukhov, V.M., Kirichenko, M.V., Khrypunova, A.L., 2021. Flexible thermoelectric module based on zinc oxide thin film grown via SILAR. Current Applied Physics 21, 121–133. https://doi.org/10.1016/j.cap.2020.10.012.

Kwon, D.K., Porte, Y., Ko, K.Y., Kim, H., Myoung, J.-M., 2018. High-performance flexible ZnO nanorod UV/gas dual sensor using Ag nanoparticle template. ACS Appl. Mater. Interfaces 10 (37), 31505–31514. https://doi.org/10.1021/acsami.8b13046.

Lee, Y.B., Kim, S.K., Lim, Y.R., Jeon, I.S., Song, W., Myung, S., Lee, S.S., Lim, J., An, K.-S., 2017. Dimensional-hybrid structures of 2D materials with ZnO nanostructures via pH-mediated hydrothermal growth for flexible UV photodetectors. ACS Applied Materials & Interfaces 9 (17), 15031–15037. https://doi.org/10.1021/acsami.7b0133010.1021/acsami.7b01330.s001.

Li, M., Zhao, M., Jiang, D., Yang, M., Li, Q., Shan, C., Zhou, X., Duan, Y., Wang, N., Sun, J., 2019. Optimizing the spacing of Ag nanoparticle layers to enhance the performance of ZnO/Ag/ZnO/Ag/ZnO multilayer-structured UV photodetectors. Sensors and Actuators A: Physical, 297, 111501-1-111501-8. doi:10.1016/j.sna.2019.07.025.

Lien, D.H., Wang, H.P., Chen, S.B. Chi, Y.-C., Wu, C.-L., Lin, G.-R., Liao, Y.-C., He, J.-H., 2018. 360° omnidirectional, printable and transparent photodetectors for flexible optoelectronics. npj Flex Electron, 2, 19-1-19-7. https://doi.org/10.1038/s41528-018-0032-2.

Ling, C., Guo, T., Shan, M., Zhao, L., Sui, H., Ma, S., Xue, Q., 2019. Oxygen vacancies of ZnO nanoparticles thin film/Si heterojunctions for ultraviolet/infrared photodetector. Journal of Alloys and Compounds. https://doi.org/10.1016/j.jallcom.2019.05.150.

Liu, S., Li, M.-Y., Su, D., Yu, M., Kan, H., Liu, H., Wang, X., Jiang, S., 2018. Broad-band high-sensitivity ZnO colloidal quantum dots/self-assembled Au nanoantennas heterostructures photodetectors. ACS Appl. Mater. Interfaces 10 (38), 32516–32525. https://doi.org/10.1021/acsami.8b0944210.1021/acsami.8b09442.s001.

Liu, Y., Zhang, X., Su, J., Li, H., Zhang, Q., Gao, Y., 2014. Ag nanoparticles@ZnO nanowire composite arrays: an absorption enhanced UV photodetector. Optics Express 22 (24), 30148–30155. https://doi.org/10.1364/oe.22.030148.

Luo, X., Zhao, F., Du, L., Lv, W., Xu, K., Peng, Y., Wang, Y., Lu, F., 2017. Ultrasensitive flexible broadband photodetectors achieving pA scale dark current. Npj Flexible Electronics 1(1), 6-1-6-6. doi:10.1038/s41528-017-0005-x.

Moreno, I., 2020. LED irradiance pattern at short distances. Applied Optics 59 (1), 190–195. https://doi.org/10.1364/AO.59.000190.

Özgür, Ü., Alivov, Y.I., Liu, C., Teke, A., Reshchikov, M.A., Doğan, S., Avrutin, V., Cho, S.-J., Morkoç, H., 2005. A comprehensive review of ZnO materials and devices. J. Appl. Phys. 98 (4), 041301. https://doi.org/10.1063/1.1992666.

Palatnik, L.S., 1983. The Structure and Physical Properties of Solids. Laboratory Manual, The School-Book, Vishcha Shkola, Kiev.

Patel, M., Pataniya, P.M., Patel, V., Sumesh, C.K., Late, D.J., 2020. Large area, broadband and highly sensitive photodetector based on ZnO-WS_2/Si heterojunction. Solar Energy 206, 974–982. https://doi.org/10.1016/j.solener.2020.06.067.

Peng, M., Wang, Y., Shen, Q., Xie, X., Zheng, H., Ma, W., Wen, Z., Sun, X., 2019. High-performance flexible and broadband photodetectors based on PbS quantum dots/ZnO nanoparticles heterostructure基于硫化铅量子点和氧化锌纳米颗粒异质结的高性能柔性和宽波段光电探测器. Science China Materials 62 (2), 225–235. https://doi.org/10.1007/s40843-018-9311-9.

Samanta, C., Bhattacharya, S., Raychaudhuri, A.K., Ghosh, B., 2020. Broadband (ultraviolet to near-infrared) photodetector fabricated in n-zno/p-si nanowires core–shell arrays with ligand-free plasmonic Au nanoparticles. The Journal of Physical Chemistry C 124 (40), 22235–22243. https://doi.org/10.1021/acs.jpcc.0c0608010.1021/acs.jpcc.0c06080.s001.

Skompska, M., Zarębska, K., 2014. Electrodeposition of ZnO nanorod arrays on transparent conducting substrates–a review. Electrochimica Acta 127, 467–488. https://doi.org/10.1016/j.electacta.2014.02.049.

Srikant, V., Clarke, D.R., 1998. On the optical band gap of zinc oxide. J. Appl. Phys. 83 (10), 5447–5451. https://doi.org/10.1063/1.367375.

Tang, H., Chen, C.-J., Huang, Z., Bright, J., Meng, G., Liu, R.-S., & Wu, N., 2020. Plasmonic hot electrons for sensing, photodetection, and solar energy applications: A perspective. J. Chem. Phys., 152(22), 220901-1-220901-21. https://doi.org/10.1063/5.0005334.

Tsybulya, S.V., Cherepanova, S.V., 2008. Introduction into Structural Analysis of Nanocrystals. Univ, Novosibirsk, Novosib. Gos.

Veerla, R.S., Sahatiya, P., Badhulika, S., 2017. Fabrication of a flexible UV photodetector and disposable photoresponsive uric acid sensor by direct writing of ZnO pencil on paper. J. Mater. Chem. C 5 (39), 10231–10240. https://doi.org/10.1039/C7TC03292G.

Wang, J., Chen, R., Xiang, L., Komarneni, S., 2018. Synthesis, properties and applications of ZnO nanomaterials with oxygen vacancies: A review. Ceramics International 44 (7), 7357–7377. https://doi.org/10.1016/j.ceramint.2018.02.013.

Wang, H.C., Hong, Y., Chen, Z., Lao, C., Lu, Y., Yang. Z., Zhu, Y., Liu, X., 2020. ZnO UV photodetectors modified by Ag nanoparticles using all-inkjet-printing. Nanoscale Res Lett., 15, 176-1-176-8. https://doi.org/10.1186/s11671-020-03405-x.

Xu, Z., Zhang, Y., Wang, Z., 2019. ZnO-based photodetector: from photon detector to pyro-phototronic effect enhanced detector. J. Phys. D: Appl. Phys., 52, 223001-1-223001-19. https://doi.org/10.1088/1361-6463/ab0728.

Xu, Y., Lin, Q., 2020. Photodetectors based on solution-processable semiconductors: Recent advances and perspectives. Applied Physics Reviews, 7(1), 011315-1-011315-21. https://doi.org/10.1063/1.5144840.

Yu, L., Mao, L., Li, Y., Li, X., Zhang, J., 2021. Solution-processed flexible $MAPbI_3$ photodetectors with ZnO Schottky contacts. Optics Express 29 (5), 7833–7843. https://doi.org/10.1364/OE.417494.

Zhai, L., Kim, H.-C., Muthoka, R.M., Latif, M., Alrobei, H., Malik, R.A., Kim, J., 2021. Environment-friendly zinc oxide nanorods-grown cellulose nanofiber nanocomposite and its electromechanical and UV sensing behaviors. Nanomaterials, 11(6), 1419-1-1419-14. https://doi.org/10.3390/nano11061419.

Zhang, Y.-Y., Zheng, Y.-X., Lai, J.-Y., Seo, J.-H., Lee, K.H., Tan, C.S., An, S., Shin, S.-H., Son, B., Kim, M., 2021. High performance flexible visible-blind ultraviolet photodetectors with two-dimensional electron gas based on unconventional release strategy. ACS Nano 15 (5), 8386–8396. https://doi.org/10.1021/acsnano.0c1037410.1021/acsnano.0c10374.s001.

Zeng, Y., Pan, X., Lu, B., Ye, Z., 2016. Fabrication of flexible self-powered UV detectors based on ZnO nanowires and the enhancement by the decoration of Ag nanoparticles. RSC Advances 6 (37), 31316–31322. https://doi.org/10.1039/C6RA02922A.

Zhou, Y.H., Zhang, Z.B., Xu, P., Zhang, H., Wang, B., 2019. UV-visible photodetector based on I-type heterostructure of ZnO-QDs/monolayer MoS_2. Nanoscale Research Letters, 14(1), 364-1 - 364-10. https://doi.org/10.1186/s11671-019-3183-8.

Zhu, T., Yang, Y., Zheng, L., Liu, L., Becker, M.L., Gong, X., 2020. Solution-processed flexible broadband photodetectors with solution-processed transparent polymeric electrode. Adv. Funct. Mater. 30 (15), 1909487. https://doi.org/10.1002/adfm.v30.1510.1002/adfm.201909487.